

# Self-organized dynamics and the transition to turbulence of confined active nematics

Achini Opathalage,\* Michael M. Norton,\* Michael P. N. Juniper, S. Ali Aghvami, Blake Langeslay, and Seth Fraden†  
*Department of Physics, Brandeis University, Waltham, MA 02453*

Zvonimir Dogic‡

*Department of Physics, University of California at Santa Barbara, Santa Barbara, CA 93106*  
(Dated: February 12, 2023)

We study how confinement transforms the chaotic dynamics of bulk microtubule-based active nematics into regular spatiotemporal patterns. For weak confinements, multiple continuously nucleating and annihilating topological defects self-organize into persistent circular flows of either handedness. Increasing confinement strength leads to the emergence of distinct dynamics, in which the slow periodic nucleation of topological defects at the boundary is superimposed onto a fast procession of a pair of defects. The defects migrate towards the confinement core over multiple rotation cycles, while the associated nematic director field evolves from a double spiral towards a circularly symmetric configuration. Spiral collapse coincides with another boundary-localized nucleation event, thus setting up long-term doubly-periodic dynamics. Experimental data is compared to existing theoretical models. Theory captures the fast procession of a pair of  $+\frac{1}{2}$  defects, but not the slow spiral collapse nor the periodic nucleation of defect pairs. Theory also fails to predict the emergence of circular flows in the weak confinement regime. The developed methods can be generalized to more complex geometries, providing a robust microfluidic platform for rationally engineering two-dimensional autonomous flows.

## INTRODUCTION

Powered by the consumption of chemical energy, active nematic liquid crystals generate mesoscopic active stresses that render the entire system unstable. For extensible nematics slight bend distortions of the director field create hydrodynamic flows that further deform the director field [1–4]. Upon saturating, these distortions produce pairs of motile topological defects that drive large-scale turbulent-like dynamics [5–15]. Design of active matter based devices that directly convert chemical energy into macroscopic mechanical work requires predictive control of the emergent spatiotemporal patterns [16–18]. In passive liquid crystals such goals can be accomplished by prescribing confinement geometry and boundary anchoring conditions, which in turn determine the configuration of the director field throughout the sample. The extent to which the dynamics of active liquid crystals can be prescribed through analogous control of the boundaries remains an open question.

We establish microfluidic methods that confine microtubule-based active nematics into domains with impermeable walls. The hard-wall boundaries enforce both the no-slip condition and the parallel anchoring that is readily described by hydrodynamic models [19–23]. Below a critical size we observe self-organized circular flows. Such flows are a ubiquitous feature of diverse experimental systems and are predicted by theoretical models [24–28]. However, experimentally identified criteria for the onset of the circular flows is fundamentally dif-

ferent from the predictions of the established theoretical models. For a subset of confinements we observe slow and highly periodic dynamics of boundary induced defect nucleation that is superimposed on the fast circular flows; a phenomena we refer to as doubly-periodic dynamics. Related dynamics has also been observed by imposing a distinct boundary condition in which the substrate has anisotropic viscosity due to a smectic substrate [29]. Taken together these observations suggest that doubly-periodic dynamics is a ubiquitous feature of confined active nematics that is not accounted for by the current theoretical models.

A long term goal of active matter research is focused on controlling autonomous motion and transport that is powered by internally generated active stresses [30, 31]. Developing predictive theoretical models is an essential stepping stone towards this goal. So far, significant effort has focused on studying the chaotic dynamics of bulk unconfined active nematics [5, 7, 8, 32, 33]. However, formulating a complete theory also requires an accurate description of boundary conditions. Our results on confined active nematics challenge existing theoretical models with data, while also identifying physical features whose inclusion into theoretical models may reconcile the observed differences.

## EXPERIMENTAL RESULTS

Using microfluidic technologies we confined active nematics into circular geometries whose diameter ranged from 60 to 800  $\mu\text{m}$  (Fig.1). For all confinements studied, microtubules exhibited parallel alignment to the boundaries, which ensured that the nematic director field contained topological defects. Specifically, disk geometry has

---

\* AO and MMN contributed equally to this work.

† fraden@brandeis.edu

‡ zdogic@physics.ucsb.edu

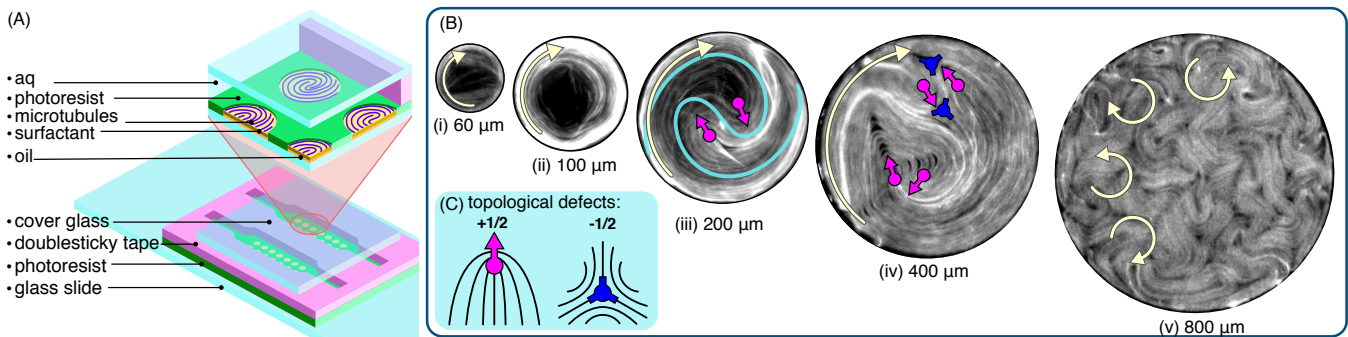


FIG. 1. **Active nematics in weak, intermediate and strong confinement regimes.** (A) Schematic of sample cell used to confine active nematic. A micro-pattern of cylindrical holes were imprinted into a photoresist layer bound to a microscope slide. Oil filling the flow chamber was displaced with an aqueous active mixture, leaving behind oil-filled holes with a circular oil-water interface located near the top of the cylindrical opening. Centrifuging microtubules onto the oil-water interface led to the formation of confined active nematic. (B) (i-v) Fluorescence images of confined active nematics with diameter ranging from 60 to 800  $\mu\text{m}$ . Yellow arrows indicate direction of circulation. Blue line overlaying 200  $\mu\text{m}$  well highlights the double spiral configuration of the nematic director observed for intermediate confinements. Photographs are not to scale. (C) Structure of nematic director field around topological defects of charge  $+\frac{1}{2}$  (magenta) and  $-\frac{1}{2}$  (blue).

an Euler characteristic of  $+1$ , thus the topological charge of all disclination defects has to add up this value [34]. For strongest confinements (60 to 100  $\mu\text{m}$ ), the diameter was less than the size of a defect in a bulk nematic (Fig.1i,ii). In this regime, microtubule bundles reduced their curvature elastic energy by migrating towards the boundaries. Consequently, the well center became devoid of filaments and developed significant density gradients. For intermediate confinements (100 to 300  $\mu\text{m}$ ), the active nematics formed two  $+\frac{1}{2}$  defects typically arranged into an asymmetric double spiral configuration (Fig.1iii). This is distinct from equilibrium nematics in which two  $+\frac{1}{2}$  defects orient along the same line, in an antipodal symmetric configuration [35, 36]. For weak confinements (300 to 600  $\mu\text{m}$ ) we observed proliferation of additional defects throughout the active nematic. In all three regimes active nematics exhibited robust circular flows. Further increasing the confinement size to 800  $\mu\text{m}$  and beyond, yielded active nematics with turbulent bulk-like dynamics. The constraint that the total topological charge adds up to  $+1$  remained intact for all confinement regimes, since nucleation events only create topologically neutral  $\pm\frac{1}{2}$  defect pairs (Fig.1iv,v).

### Intermediate confinements

We first describe dynamics of active nematics in intermediate confinements, which exhibited persistent circulating flows accompanied by complex, but highly periodic dynamics of topological defects (Movie S1, S2). From a time sequence of fluorescently acquired images we extracted the spatiotemporal evolution of the nematic director field (Fig. 2A), and using a previously developed algorithm we identified the locations of the topological defects [13]. Immediately before a boundary nucleation

event, the two circulating  $+\frac{1}{2}$  defects almost merged at the center, and the director field adopted a circularly symmetric configuration (-2.5 s in Fig.2A). This configuration was unstable and the effective defect merger at the confinement core coincided with initiation of a remote event at the boundary (0-5 s in Fig. 2A). Specifically, over the next few seconds, the boundary-adjacent microtubule layer underwent a large scale inward buckling deformation that was driven by the intrinsic bend instability of extensile active nematics. As the instability grew it generated a pair of  $\pm\frac{1}{2}$  defects. The  $+\frac{1}{2}$  defect was propelled towards the center, while the oppositely charged  $-\frac{1}{2}$  defect remained at the boundary, eventually merging with one of the two original  $+\frac{1}{2}$  defects (5-10 s in Fig. 2A). The boundary nucleation event briefly disrupted the regular procession of the defects, but within a short time the active nematic reestablished the spiral configuration that powered robust circular flows. The periodicity of these flows was  $\sim 10$  s, as can be seen by plotting the angular position of the  $+\frac{1}{2}$  topological defects (Fig. 2C). Over multiple rotations the pair of defects, arranged in a double spiral, slowly migrated towards the center (Fig. 2B). This inward winding and the associated collapse of the spiral reconfigured the nematic director field, recreating the circularly symmetric configuration (44 s in Fig. 2A), which initiated another boundary induced nucleation event, thus setting up long-term periodic dynamics.

The above described dynamics of the confined active nematics were coupled to spatiotemporal changes in the local microtubule density. Simultaneous with the inward defect movement, driven by extensile stresses microtubules migrated outward (Fig. 2D). As the  $+\frac{1}{2}$  defect detached from the boundary, it repopulated the confinement center with filaments. It also pulled along a bright thread of microtubules, which served as a tracer for the

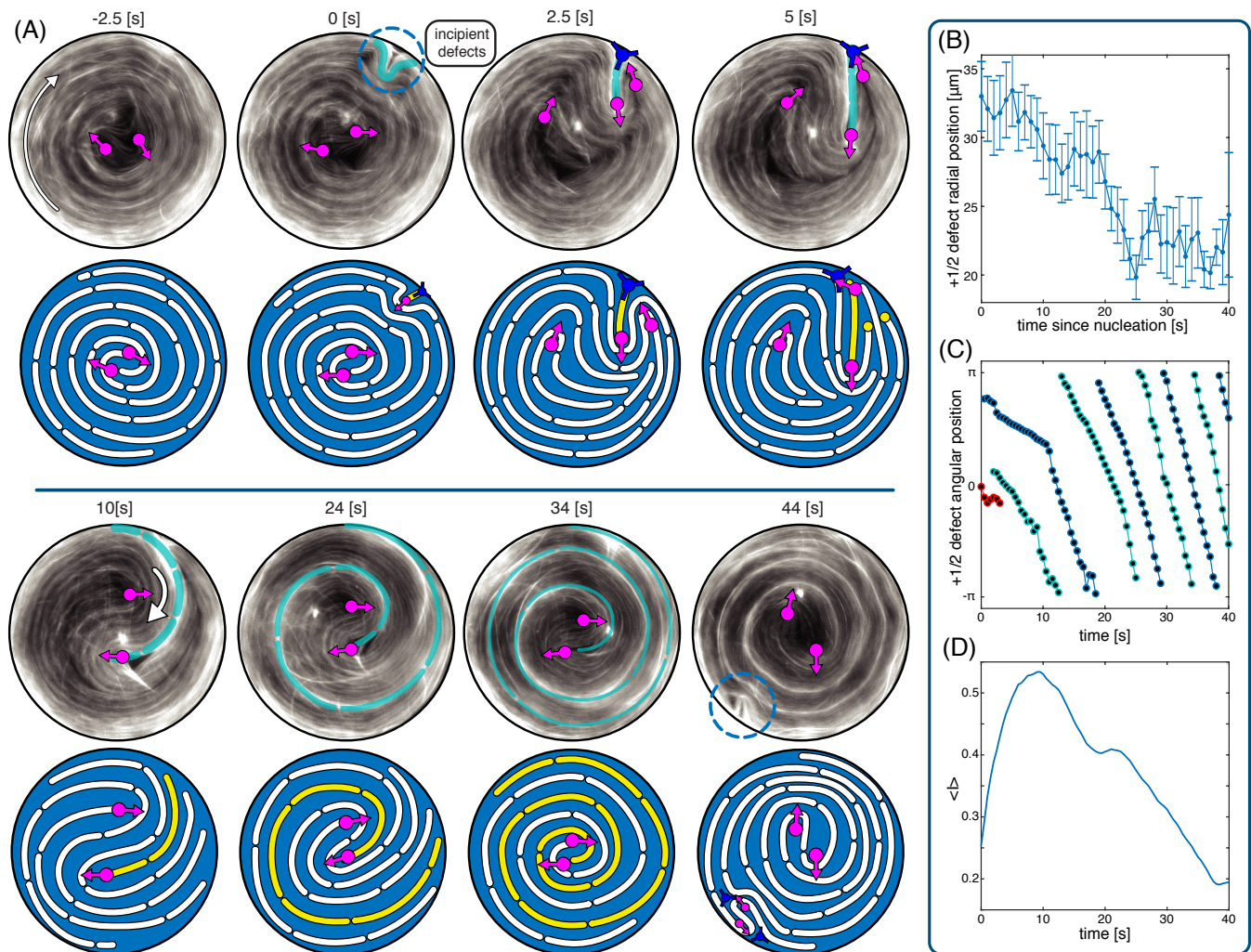


**FIG. 2. Dynamics of confined active nematic at intermediate confinements (A)** Fluorescent images and accompanying illustrations depict the spatiotemporal evolution of the nematic field during one cycle consisting of boundary induced defect nucleation and subsequent spiral collapse. (-2.5 s) The system begins in a nearly circularly symmetric state. (0 s) Microtubules adjacent to the boundary buckle, creating a defect that travels inwards. (2.5 s - 5 s) A fracture forms between the  $-\frac{1}{2}$  defect created during nucleation and one of the original  $+\frac{1}{2}$  defects, returning the system to a two-defect configuration. (10 s - 34 s) A pair of orbiting  $+\frac{1}{2}$  defects approach each other over multiple rotations. (44 s) The confined active nematic returns to the original almost perfectly circular configuration. Over next few seconds the microtubule layer once again buckles. Another cycle is shown in Fig. S2 and dynamics are shown in movie S2. **(B)** Radial position of  $+\frac{1}{2}$  defects as a function of time shows the inward defect migration. The defect position was averaged over twenty cycles. The radial position increases towards the end of the cycle as buckling begins to push the existing defects out of the center. Error bars are standard error. **(C)** Angular position of  $+\frac{1}{2}$  defects during one defect nucleation cycle is indicative of the fast procession with a  $\sim 10$  s period, colors indicate different defects. **(D)** Fluorescence intensity, averaged over the central area with  $50\mu\text{m}$  diameter. Defect nucleation repopulates the disk interior with microtubules for first 10 s; afterwards the microtubule density steadily decreases as the the defects circulate and filaments are expelled towards the boundary (10 s - 40 s). Confinement diameter is  $200\mu\text{m}$ .

deformations undergone by a material element in the nematic. As defects precessed around each other along a collapsing double spiral, this thread continuously elongated, winding around the center multiple times (cyan line in Fig. 2A). Notably the two defects arranged at the core of double spiral never crossed the elongating thread. The outward migration was reversed by a subsequent boundary induced defect nucleation that pushed

microtubules inward, thus initiating another cycle.

Following the system on longer time scales revealed that the above described dynamics repeated itself with a period of  $\sim 40 \pm 5$  s (Fig. 3A, B). Time evolution of the angular defect position confirmed that the slow nucleation dynamics was superimposed on much faster circular flows, in which defects completed a circular orbit with a  $\sim 10$  second period (Fig. 3D). In the fast majority

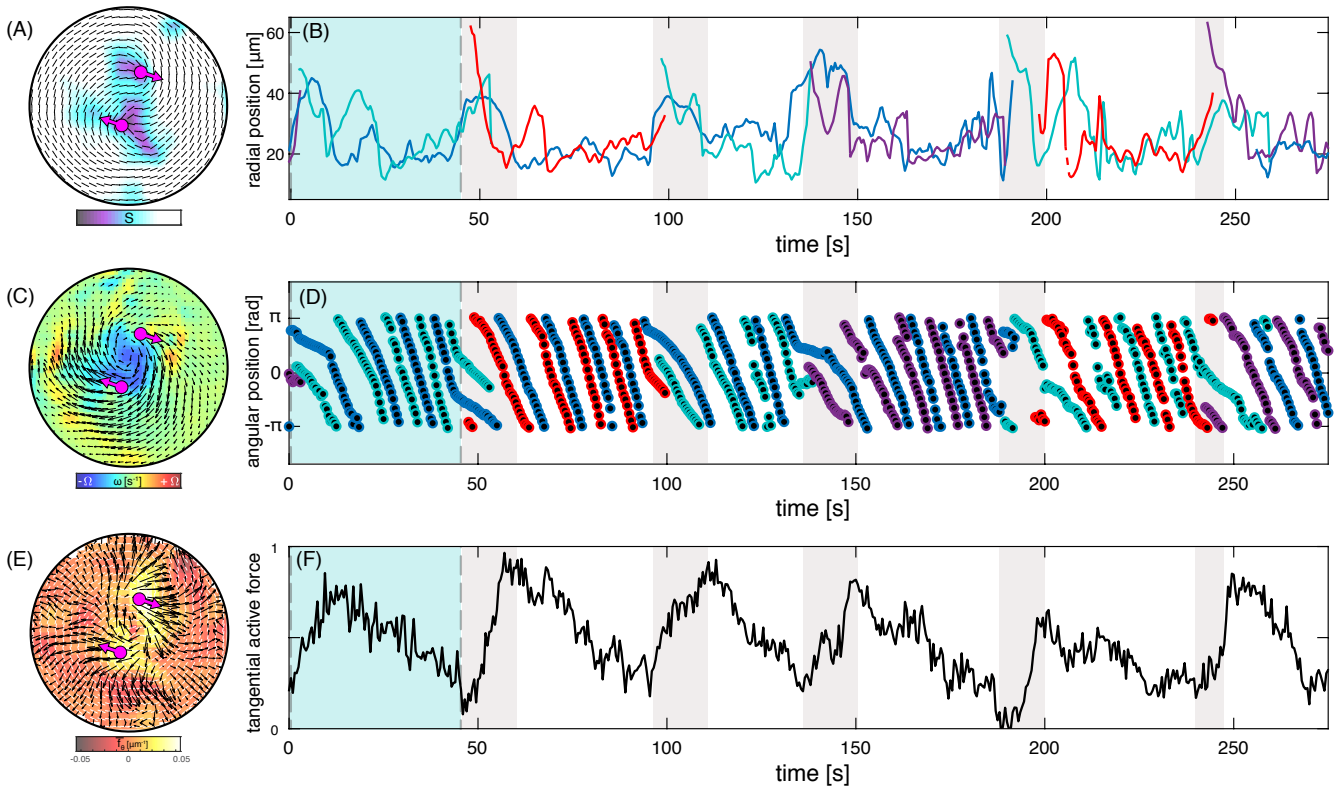


FIG. 3. **Long-time periodic dynamics at intermediate confinements.** (A) Map of the director field  $\mathbf{n}$  and associated order parameter  $S$  extracted from fluorescence images.  $+\frac{1}{2}$  defects are also shown. (B) Radial position of  $+\frac{1}{2}$  defects plotted over several boundary nucleation events (period  $\sim 50$  sec) and many defect orbit periods (period  $\sim 10$  sec). Colors indicate different defects. (C) PIV analysis yields a map of the autonomous flow and vorticity field (vorticity scale  $\Omega = \pm 0.8 \text{ sec}^{-1}$ ). (D) Angular position of  $+\frac{1}{2}$  defects. The unchanging sign of the slope indicates that handedness of the circulation persists over multiple cycles of defect nucleation. Colors indicate different defects. (E) Spatial map of the active force  $\bar{\mathbf{f}} = \mathbf{f}/\alpha = \nabla \cdot \mathbf{Q}$  normalized by unknown activity parameter  $\alpha$  (black arrows) and the magnitude of tangential component  $\bar{\mathbf{f}} \cdot \hat{\mathbf{e}}_\theta$  (color field). (F) Spatially integrated total active force in the tangential direction  $\int d\mathbf{x} \bar{\mathbf{f}}_\theta$  as a function of time. Maxima correspond to configurations where the two  $+\frac{1}{2}$  defects are far from one another, minima occur directly before nucleation when defects have effectively merged. Scale is normalized by  $64 \mu\text{m}$ . Images in panels (A), (C), and (E) correspond to Fig. 2A ( $t=10$  s). The light blue shaded window in (B),(D),(F) corresponds to snapshots in Fig. 2A. The grey shaded windows indicate nucleation events. Confinement diameter is  $200 \mu\text{m}$ .

of the cases the boundary induced defect nucleation preserved the flow handedness, although on the rare occasion reversal of the spontaneous circular flows was observed (at 4300 seconds in movie S1). We have also used particle imaging velocimetry (PIV) to characterize the circular flows (Fig. 3C). However, caution needs to be taken when interpreting these results since the PIV algorithm does not track dynamics that are tangent to uniformly aligned regions; thus such data is semi-quantitative.

To gain insight into the mechanisms underlying the doubly-periodic dynamics, we extracted active stresses from the evolving nematic director field. Hydrodynamic theory postulates that these stresses are proportional to the nematic order tensor  $\mathbf{Q}$ . Thus, the force that drives the autonomous flows is related to the gradients of the active stress, and regions of spatially varying nematic order are required to generate flows [1, 2]. From the experimentally measured map of the nematic director field we

estimated both the active force  $\mathbf{f} \propto \nabla \cdot \mathbf{Q}$  (arrows in Fig. 3E) and the component that drives azimuthal circulating flows,  $\propto \hat{\mathbf{e}}_\theta \cdot \nabla \cdot \mathbf{Q}$  (heat map in Fig. 3E). Since prefactor  $\alpha$  that relates the nematic tensor to the active stress is unknown, we report  $\bar{\mathbf{f}} = \mathbf{f}/\alpha$ . The initial asymmetric spiral director field generated significant gradients of stress in the azimuthal direction, which in turn powered strong circular flows (Fig. 3F,  $t=10$  s). The evolution of the systems towards a configuration with a more pronounced circular symmetry reduced the magnitude of this force. The boundary induced defect nucleation correlated with the time point where the active force reached a minimum. This suggests that sufficiently strong flow alignment generated by the circular flows suppressed nascent defects that might otherwise form through the bend instability. Only once these flows were sufficiently weak due to the collapsing spiral could the boundary induced defect nucleation proceed.

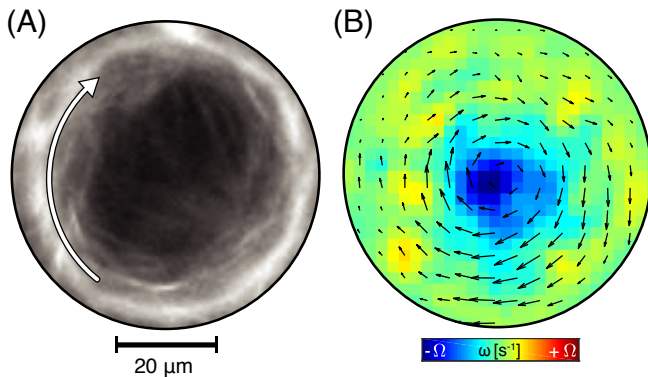


FIG. 4. **Active nematics in strong confinement (A)** Circulating fluorescently labeled microtubules confined to a  $60 \mu\text{m}$  diameter well (Movie S4). **(B)** Time-averaged (25 seconds) flow field and vorticity,  $\Omega = \pm 0.19 \text{ s}^{-1}$ .

### Transition to strong confinements

Doubly-periodic dynamics associated with the intermediate confinements persisted as the diameter was reduced below  $200 \mu\text{m}$ . However, for  $100 \mu\text{m}$  confinements the dynamics exhibited new behaviors. In this regime confinement size is comparable to the defect core size (Movie S3). Consequently, microtubule accumulation along the boundary became increasingly prominent. The center of the disk, if it contains microtubules at all, often exhibited simple rigid body rotation, driven by the boundary. Reducing the confinement size further to  $60 \mu\text{m}$  accentuates these behaviors (Fig. 4, Movie S4). In this case the extending bundles no longer formed a continuous nematic field, but a fragmented ring at the boundary, while leaving large voids in the center. The temporal dynamics was no longer continuous and regular. Despite the loss of some structural order, we still observed fairly consistent circular rotations and intermittent buckling events. It is likely that the continuum approximation is no longer valid in this limit. Theory predicts that for small enough confinements, net circulation ceases because the active stresses are not strong enough to overcome the elastic distortions [22]. In our experiments, we never observed this prediction.

### Weak confinements

Active nematics confined to circles with diameter between  $400$  and  $600 \mu\text{m}$  exhibited qualitatively new behavior compared to the intermediate confinement case, as defects nucleated both at the boundary and within the interior (Fig. 5A). Consequently, in addition to the two topologically required  $+\frac{1}{2}$  defects, at most times the system contained several additional defect pairs, whose number fluctuated anywhere between 2 and 10 (Fig. 5B). Except for short term errors in defect tracking, the net charge of all defects added up to  $+1$ . Visual inspection

revealed that these samples still exhibited coherent circular flows despite the presence of additional defects (Movie S5). To quantify this phenomena, we defined the signed order parameter that indicates the degree of flow circulation as  $\Phi(t) = \langle \mathbf{u} \cdot \hat{\mathbf{e}}_\theta / |\mathbf{u}| \rangle$ , where  $\mathbf{u}$  is the velocity field extracted from the PIV algorithm (Fig.5C).  $\Phi = \pm 1$  indicates system-scale coherent circular flows, while  $\Phi = 0$  indicates lack of any net transport along the azimuthal direction [28, 37]. Temporal evolution of the flow order parameter confirms that weakly confined active nematics exhibited persistent circular flows that switched handedness on the timescales of tens of minutes (Fig.5D).

### Transition to bulk turbulence

So far we described the dynamics of active nematics in confinements ranging from  $60$  to  $600 \mu\text{m}$ . For intermediate confinements, dynamics consisted of periodic boundary nucleation and the slow inward spiral collapse that was superimposed on faster circular flows. For larger diameter wells (weak confinement), circular flows persisted, but defects nucleated both at the boundary and within the interior, and the nucleation dynamics was no longer deterministic, but rather chaotic. The transition between these regimes was gradual. To compare the behavior across all lengthscales we plotted the time-averaged flow order parameter  $\langle |\Phi| \rangle_t$  against the confinement size (Fig. 6A). Self-organized circular flows had the same degree of flow order for confinements up to  $600 \mu\text{m}$ . Beyond this size  $\langle |\Phi| \rangle_t$  dropped to zero, indicating the transition to bulk-like chaotic dynamics (Movie S6).

Motivated by the close relationship between topological defects and autonomous flows we examined how the defect density depends on the confinement size. In bulk active nematics, active stresses generate topological defects and their magnitude determines the preferred defect density. Reducing the confinement diameter leads to an increase of the effective density, since topological constraints ensure formation of at least two  $+\frac{1}{2}$  defects, even for confinements smaller than the average bulk defect spacing. Plotting the average defect density as a function of the confinement size reveals the expected increase for geometries less than  $\sim 200 \mu\text{m}$  (Fig. 6A), which is comparable to the length scale extracted from the analysis of bulk active nematics [38]. Therefore, from a structural perspective, active nematics become unconfined above  $\sim 200 \mu\text{m}$ . In contrast, the dynamical signature of confinement as manifested by the emergence of circular flows, persists for much weaker confinement, remaining even as the diameter is increased to  $\sim 600 \mu\text{m}$  (Fig. 6A).

We compared these findings to predictions of the hydrodynamic theories which examined emergence of flows in confined active nematics [19, 21, 22, 39]. To make a meaningful comparison to experimental data, we used a theoretical model described elsewhere to determine how the defect density and the flow order parameter change

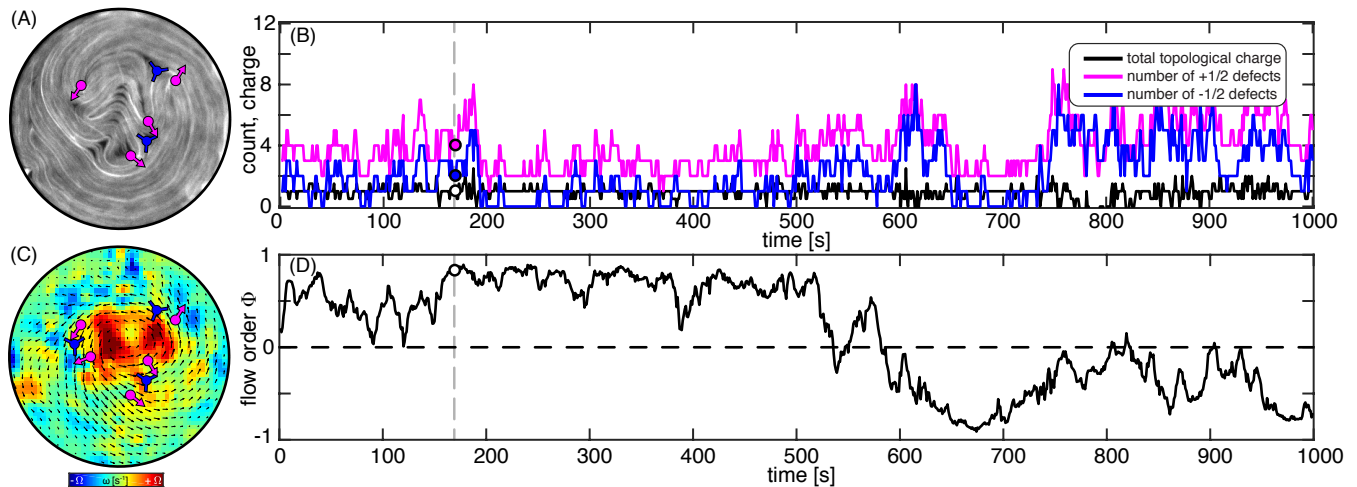


FIG. 5. **Active nematics in weak confinement** (A) Fluorescence image of an active nematic in the regime where topological defects nucleate both in the interior and at the boundary; the  $+1/2$  defects are predominantly aligned along the flow direction. (B) Time evolution of the number of  $+1/2$  defects (magenta),  $-1/2$  (blue), and the total topological charge (black). The total charge remains +1 except for short-time tracking errors. (C) Spatial map of the instantaneous flow field and vorticity (vorticity scale is  $\Omega = \pm 0.27 \text{ s}^{-1}$ ). (D) Time evolution of the flow order parameter demonstrates that the circular flows with specific handedness persist for periods up to 10 minutes. The vertical line in (B) and (D) corresponds to the time in (A) and (C). Confinement diameter is  $400 \mu\text{m}$ .

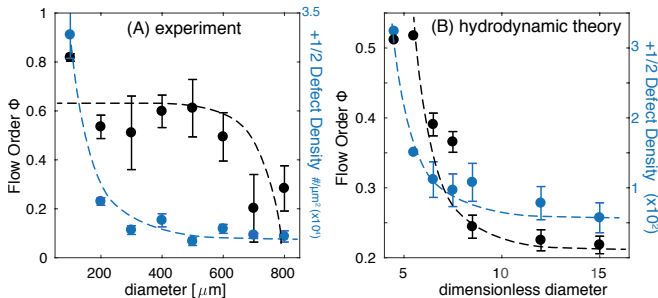


FIG. 6. **Dynamical and structural criteria for the onset of circular flows** (A) Experimentally measured flow order parameter (black) and  $+1/2$  defect density (blue) is averaged over sample lifetimes and plotted as a function of the confining disk radius. The onset of circular flows is observed for  $600 \mu\text{m}$  confinements, while the topological constraints modify the average defect density for confinements below  $200 \mu\text{m}$ . Error bars represent standard error across different wells. (B) Theoretical predictions of the flow order parameter and defect density plotted as a function of disk size for dimensionless activity  $\alpha=10$ . The onset of circular flows is tightly coupled to the increase of the defect density. Error bars represent standard error with  $n = T/\tau$  measurements where  $T$  is the simulation duration and  $\tau$  is the average lifetime of a defect.

with the confinement size (Fig.6B) [22]. Theory predicts that the onset of the circular flows coincides with the increase in the effective defect density. Equivalently, circular flows appeared only when the system was confined below the defect spacing preferred by the bulk samples. Increasing the confinement size to the point where any additional defects appear immediately suppressed circu-

lar flows. This is in contrast to experiments where active nematics exhibited robust circular flows even in the presence of several additional defect pairs. Thus, theory predicts that the transition to bulk behavior and turbulence occurs by a one step transition characterized by concomitant changes in defect density and flow order, while in experiment the structural and dynamic transitions occur at different diameters (Fig. 6A and 6B).

We examined an additional structural aspect of confined active nematics by plotting the time-averaged radial distribution of  $+1/2$  defect density for different confinement sizes (Fig. 7A). For moderately confined active nematics, the topological constraints gave rise to a defect density distribution with a peak at a well-defined radial position. Intriguingly, the radial position of the peak did not significantly change, even as the confinement diameter increased from  $100$  to  $300 \mu\text{m}$ . Beyond this diameter the peak in the radial density distribution disappeared. This drop coincides with the onset of the weak confinement dynamics in which defects proliferate but long-time circulation persists (Fig. 5). In this regime the measured probability distribution was flat over the inner part of the disk, and decayed to almost zero upon approaching the boundary.

Theoretical predictions capture both the sharp peak at strong confinements, and the flattening of the distribution as confinement diameter is increased (Fig. 7B, [22]). However, the details of the predicted defect distribution diverge subtly from the experiment; theory predicts that the maximum of the distribution moves outward with increasing confinement size, in contrast to experimental observations of a fairly large boundary exclusion zone

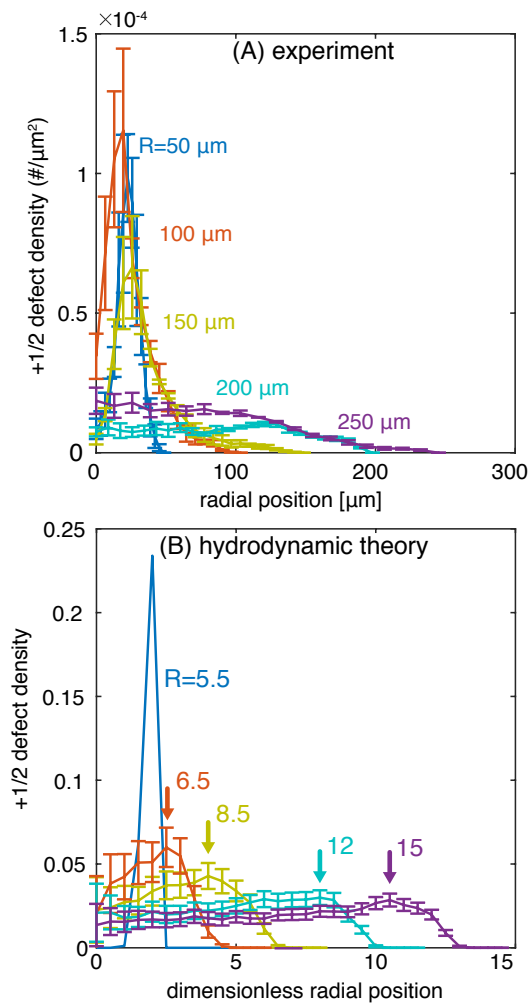


FIG. 7. **Radial distribution of defect densities for different confinement regimes (A)** Time averaged radial distributions of  $+\frac{1}{2}$  defects plotted for confinements of different radii. For stronger confinements the topological constraint requires presence of two  $+\frac{1}{2}$  defects regardless of the energetic penalty, giving rise to a sharp peak in the defect density distribution at a well-defined radius. Error bars represent standard error across different wells. **(B)** Theoretically calculated defect distribution plotted as a function of confinement size for dimensionless activity  $\alpha=10$ . In small diameter wells, defects orbit at a preferred radius. In larger diameter wells, defects tend towards uniform density in the well interior with a local maxima (arrows) near the hard wall boundary [22]. Error bars represent standard error with  $n = T/\tau$  measurements where  $T$  is the simulation duration and  $\tau$  is the average defects lifetime.

with low defect density. This suggests that the dynamics that direct the  $+\frac{1}{2}$  defects towards the center at intermediate confinement (described in Fig. 2) are also relevant for larger diameters, transporting defects towards the interior of the well.

To gain insight into the discrepancy between theory and experiments, we examined defect motion subsequent

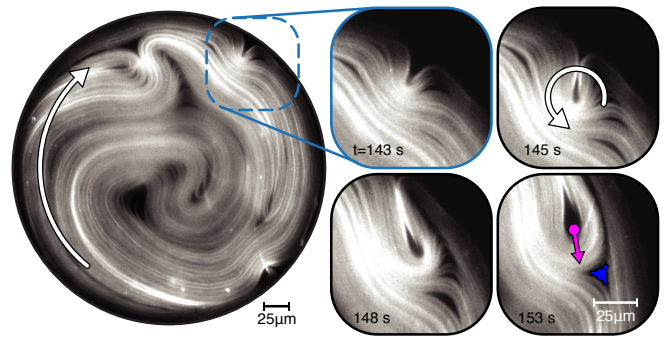


FIG. 8. **Temporal evolution of boundary-nucleated defects.** Persistent clockwise flows of defect-laden nematic in a weak confinement regime (movie S7). Inset: Defects nucleated at the boundary rotate and align with the existing director field reinforcing the circulation. These dynamics consistently produce  $\pm\frac{1}{2}$  pairs featuring a  $+\frac{1}{2}$  defect that pushes its oppositely charged counterpart before annealing. Confining diameter,  $300 \mu\text{m}$

to their boundary nucleation. Initially, the instability grows perpendicular to the boundary. In isolation a nucleated  $+\frac{1}{2}$  defect is most likely to move towards the center. However, existing circular flows and the associated nematic director field rapidly reorient the newly created defects in the azimuthal direction (Fig. 8). Defects with such alignment generate additional active stresses that further stabilize circular flows. Furthermore, evolving dynamics leads to the creation of a novel compound defect structure composed of a  $+\frac{1}{2}$  defect with a  $-\frac{1}{2}$  defect ( $t=153$  s Fig. 8). Together, the defect pair acts as an active wedge that both drives the circulation and splays the nematic. The pair of defects has a substantial lifetime before annealing (Movie S7). Microtubule based active nematics can be considered polymer liquid crystals. Consequently, for defect annihilation to take place the material in front of the anisotropic  $+\frac{1}{2}$  has to be expelled, in contrast to low molecular weight liquid crystals where reorientation of the director would suffice to anneal defect pairs. These effects are not accounted for in the current theoretical models of defect interactions [5, 9, 40]

### Non-circular geometries

So far we described dynamics of circularly confined active nematics. However, the developed experimental methods are more general and can be used to study dynamics in diverse confined geometries. To demonstrate their potential we confined active nematics within a disk with an inward notch, an annulus, and rectangular boxes of different lengths and widths. A chiral notch at the confining boundary of a disk controls the spatial location of defect nucleation (Movie S8). It also ensures that autonomous flows have only one handedness, which is reminiscent of the methods that control the flow of 3D isotropic active fluids [28]. Our experiments show

that confining active nematics within an annulus provides an alternate method of engineering coherent long-ranged flows (Fig. 9A, Movie S9). It remains an important question to determine how the annular width determines the structure of the self-organized flows. We also observed intriguing dynamics in active nematics confined within a rectangular box with a large aspect ratio (Fig. 9B, Movie 10). For the majority of the time the dynamics of this system is chaotic. However, occasionally we observed an organized state in which defects collectively and simultaneously nucleated at the boundary and subsequently propagated into the interior.

## DISCUSSION AND CONCLUSION

Persistent circular motion has been observed in a wide range of confined active matter systems ranging from clusters of motile eukaryotic cells, and dense bacterial suspensions to synthetic motile colloids [24, 28, 41–44]. All of these systems are characterized by a single time scale related to the frequency of rotational motion. Our observations confirm the universality of circular flows in confined active matter. However, when compared to previous experiments, as well as to predictions of continuum models, our findings also demonstrate an unexpected complexity in the self-organized dynamics of confined microtubule-based nematics. In particular, defects nucleated at a boundary subsequently formed a double spiral that slowly shrank over multiple rotation cycles. The collapsing double spiral, once sufficiently circular, was reconfigured by another boundary nucleation event that set up the doubly-periodic dynamics.

While the exact experimental factors that control the onset of defect nucleation remain unknown, our observations suggest two mechanisms. One possibility is that the build-up of the microtubule density at the edge increases local active stresses. Once these reach a critical magnitude the generic nematic instability develops, leading to boundary induced defect formation. Another possibility is that defect nucleation is suppressed by the persistent circulating flows that tend to align the director azimuthally. As the double spiral collapses, there is a marked decrease in the total active force generated in the azimuthal direction, which presumably leads to the slowdown of the associated flows. Once they decrease below a certain threshold, the flows no longer suppress defect nucleation. This disinhibition initiates another cycle of defect dynamics. These two mechanisms are not mutually exclusive; both increased activity and weakened suppression of defect nucleation could be experimentally relevant to triggering the temporal onset of defect nucleation events.

Dynamics similar to those described here have been observed in active nematics assembled on smectic focal-conic domains which provide soft circular confinement [29]. In both cases there is pronounced migration of microtubules from the high-curvature interior to the

lower-curvature boundaries. However, the dynamics that disrupt the circular structure in the two systems are distinct. The smectic-confined circular nematics lose stability along the entire periphery with a well-defined wavelength. In contrast, the hard-wall boundary provides additional viscous drag and prevents outward buckling, causing nucleation to occur as a distinct, spatially localized event that produces a single  $\pm\frac{1}{2}$  defect pair.

Using confinements of increasing diameter we studied the transition from the doubly-periodic dynamics to turbulence, observing that it takes place in two steps. Weakening confinement by increasing diameter above a first threshold leads to a profusion of additional defects beyond the minimum number required by topology. Defects nucleated both at the boundary and the interior, and the density of defects approached the value measured in bulk. However, the flow remained circular and highly ordered. Only by weakening confinement further beyond the second threshold diameter did the circular flows cease and the dynamics of the bulk active nematic appear. Existing continuum theories fail to predict either the intermediate doubly-periodic dynamics or a two-step route to bulk-like turbulence [7, 19–23, 39]. Our observations indicate that the long range spatial extent of microtubule bundles that are organized into threads constrain active nematic dynamics in complex ways. Strong non-local interactions are absent from current models, but might be essential for formulating predictive theories.

In summary, we have demonstrated that confinement effectively transforms the dynamics of active nematics, including formation of self-organized doubly-periodic spatiotemporal patterns. These observations raise an interesting question about the extent to which the dynamics of active nematics can be rationally engineered by tuning confinement geometry. Answering this question requires both further experimental explorations, as well as development of theoretical models that more accurately account for the experimentally observed realities of defect nucleation and interactions. More broadly, the dynamics of our reconstituted minimal system is evocative of the phenomena observed in living organisms, which frequently exhibit complex spatiotemporal patterns that emerge on lengthscales and timescales that are significantly larger than the size and the lifetime of the biochemical constituents [45]. Using kinesin motors that take an 8 nanometer sized step every ten milliseconds, we demonstrate self-organized spatiotemporal patterns with lifetimes of minutes on lengthscales of hundreds of microns. Understanding the fundamental organizing principles that drive the dynamics of active nematics might reveal general strategies for rationally engineering adaptable and dynamical synthetic materials with biomimetic capabilities.



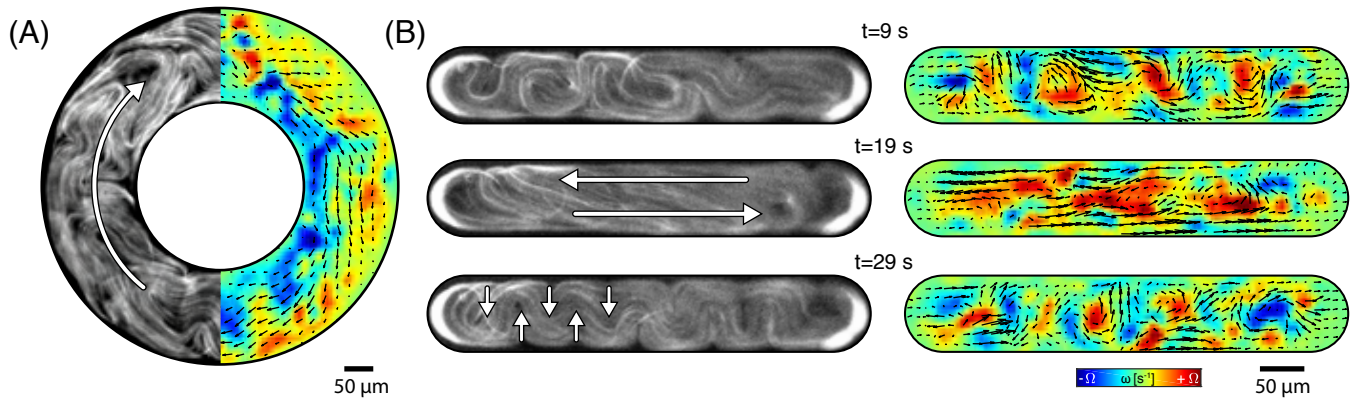


FIG. 9. **Active nematics in complex geometries.** (A) Active nematic confined in an annulus with  $150 \mu\text{m}$  width. Fluorescently labeled microtubules are shown on the left and the flow field extracted from the PIV analysis is shown on the right half. Temporal evolution is shown in movie S9. (B) Dynamics of microtubule active nematics in rectangular confinements. Left column shows evolving structure of the nematics field. Velocity field shows the destruction and re-creation of a single row of vortices with alternating sign. Temporal evolution is shown in movie S10.

## METHODS

### Microtubule based active nematics

We used active nematics comprised of three components: GMPCPP stabilized microtubules labeled with Alexa 647 dye, biotin labeled kinesin-motors bound into multi-motor clusters by tetrameric streptavidin [46], and a depletion agent that induces microtubule bundling while still allowing for their relative sliding [47–49]. Kinesin clusters simultaneously bind multiple microtubules in a bundle, and depending on their relative polarity drives the bundle extension [12]. Following previous work, we sediment the extensile bundles onto a surfactant stabilized oil-water interface where they assemble into a dense quasi-2D active nematic film. The aqueous suspension also contained an ATP regenerating system to increase the experimental life-time and an antioxidant system to prevent photobleaching [12, 13]. Depending on the source of the kinesin motor proteins and microtubules the dynamics of active nematic can vary significantly. Similarly we found that these parameters greatly affected the frequency of circulating active nematics. However, they did not affect the confinement size where dynamics transitions between strong, intermediate and weak regimes.

### Fabricating micro-chambers for confinement

An array of circular micro-chambers with diameters that ranged from  $60 - 800 \mu\text{m}$  were fabricated on glass microscope slides using standard photolithography techniques, (Fig. 1A). The  $3 \times 4$  inch microscope glass slides were pre-cut to  $3 \times 3$  inch using a diamond tip scribe, in order to fit them in the vacuum chuck of the mask aligner. The slides were then rinsed and sequentially sonicated

with (1) hot water containing 0.5% detergent (Hellmanex III, Hellma Analytics), (2) then with ethanol, and (3) finally with 0.1 M NaOH. In order to enhance SU8 bonding to glass, the slides were immersed in a silane mixture consisting of 98% deionized water, 1% acetic acid and 1% (3-aminopropyl) trimethoxysilane (Sigma Aldrich) for 20 minutes. Slides were then rinsed with deionized water, dried with  $\text{N}_2$  gas and placed on a hot plate at  $180 \text{ C}$  for 15 minutes to remove moisture. Once cooled, photoresist SU8 3025 (MicroChem Corp.) was spin-coated on the slides at 1400 rpm (Headway Research). Subsequent standard photolithography processing steps, including soft baking for 20 mins at  $95 \text{ C}$ , UV exposure through a photomask with  $180 \text{ mJ/cm}^2$  and post exposure baking for 10 minutes at  $95 \text{ C}$ . Photoresist development was carried out on the slides followed by hard-baking for 30 minutes at  $180 \text{ C}$ . The depth of the micro-chambers was  $\sim 30 \mu\text{m}$  as measured by an optical profilometer.

### Assembling the flow cell and confining the active nematics

In order to prevent non-specific adsorption of microtubules and motors and to create a hydrophilic surface, the lithographed microscope glass slides and no. 1.5 coverslips were plasma etched and coated with polyacrylamide as described elsewhere [50]. Subsequently, each slide was rinsed and dried with  $\text{N}_2$  gas immediately before use. Polyacrylamide treated lithographed slides and cover slips were assembled into a flow cell using  $\sim 100 \mu\text{m}$  thick double-sided transfer tape (3M 93005LE) with laser-cut flow channels. HFE7500 oil (3M) with 1.8% (v/v) Fluoro-surfactant (RAN Biotechnologies) was flowed into the cell. Subsequently, the aqueous active mixture was flowed through the channel, displacing the

oil-surfactant mixture from all but the hydrophobic SU8 micro-chambers. The flow channel was then sealed with optical UV curable glue and centrifuged at 1000 rpm for 10 min using a Sorval Legend RT (rotor 6434) to drive the bundled microtubules onto the surfactant-stabilized oil-water interface. Within each sample on average about 20% of wells had well-defined circularly confined active nematic. Fluorinated oil often wetted areas of the SU8 photoresist, leading to the regions that formed bulk-like unconfined active nematics. However, since there were several hundred micro-chambers per slide and less than 10 could be imaged during the lifetime of the active nematic, the 20% success rate was sufficient.

### Imaging confined 2D active nematic

The confined active nematic was imaged using a wide-field fluorescent Nikon Eclipse Ti-E microscope with an Andor Clara camera controlled by Micromanager open-source software. The dynamics of quasi 2D active nematics is dependent on the thickness and concentration of microtubule film, the product of which is proportional to the optical retardance, which was determined with an LC-PolScope module [13]. Birefringence of the SU8 photoresist limited our ability to quantify the retardance of the confined active nematic. In order to avoid spillover of signal from the SU8 periphery, the field aperture was partially closed to image about three quarters of the confined area. These measurements determined the upper bound of the retardance of the nematic to be about a nanometer, which is close to the retardance resolution limit. Because of the small ratio of signal to noise, we could not quantitatively compare the retardance of the contents of the wells across experiments.

### Image Processing of the Director Field

In contrast to previous studies, the high birefringence of SU8 photoresists precludes the use of the LC-PolScope to directly quantify the director field [13]. Instead, the director field was extracted from fluorescent images. The nematic order tensor,  $\mathbf{Q} = \mathbf{n} \otimes \mathbf{n} - \frac{1}{2}\mathbf{I}$ , was constructed by finding the direction  $\mathbf{n}$ , perpendicular to the principal direction of the structure tensor of the image  $\nabla I \otimes \nabla I$ , where  $I$  is image intensity pixel value [14]. The degree

of order,  $s = 2 \text{Tr} \langle \mathbf{Q} \rangle^2$ , was found by averaging  $\mathbf{Q}$  over a small region. To avoid assigning nematic order to regions that are largely devoid of microtubules, the displayed scalar order parameter field  $S$  was weighted by the image intensity ( $I$ ) if the pixel value was below 10% of the maximum ( $I_{\text{max}}$ );  $S = s * I / I_{\text{max}}$ , with  $s$  the unweighted order parameter. Defects in the director field were found using a previously developed algorithm [13]. Defect tracking errors for the data set represented in Fig. 5 are shown in the electronic supplement, Fig. S2.

### Processing of the Flow Field

The velocity field  $\mathbf{u}$  was found by applying particle image velocimetry analysis to the fluorescently labeled microtubules using the MatLab plug-in PIVlab v1.43 [51]. In typical PIV applications, the flow is quantified by following sparsely labeled, small, isotropic tracer particles. Since these conditions would decrease the quality of the measured director field, PIV analysis is performed on densely labelled microtubules. Consequently, velocity components parallel to the director are under-sampled. For example, since the nematic is nearly parallel along the boundaries, we expect the PIV analysis to underestimate the tangential flows in these regions and consequently, the order of tangential flow ordering  $\Phi = \langle \mathbf{u} \cdot \hat{\mathbf{e}}_{\theta} / |\mathbf{u}| \rangle$  discussed in the text. We were still able to detect circulation in many cases because  $+\frac{1}{2}$  defects dominate motion. They feature a nematic field perpendicular to the direction of their motion, which is well captured by the PIV algorithm.

### ACKNOWLEDGEMENTS

We acknowledge useful conversations with Michael Hagan, Aparna Baskaran, and Stephen DeCamp. Experimental analysis of circular confinements was supported by Department of Energy of Basic Energy Sciences, through award DE-SC0010432TDD. Development of microfluidic confinement technology and extension to non-circular geometries was supported by Brandeis MRSEC through grant NSF-MRSEC-1420382. We also acknowledge the use of a MRSEC optical, microfluidic and biosynthesis facility supported by NSF-MRSEC-1420382. Development of the computational model of confined active nematics was supported by NSF-DMR-1810077.

---

[1] R. Aditi Simha and S. Ramaswamy, Physical review letters **89**, 058101 (2002), arXiv:0108301v2 [arXiv:cond-mat].  
 [2] M. C. Marchetti, J. F. Joanny, S. Ramaswamy, T. B. Liverpool, J. Prost, M. Rao, and R. A. Simha, Reviews of Modern Physics **85**, 1143 (2013), arXiv:1207.2929.  
 [3] S. Ramaswamy, Annual Review of Condensed Matter Physics **1**, 323 (2010).

[4] M. J. Shelley, Annual Review of Fluid Mechanics **48**, 487 (2016).  
 [5] L. Giomi, M. J. Bowick, X. Ma, and M. C. Marchetti, Physical Review Letters **110**, 228101 (2013), arXiv:arXiv:1303.4720v2.  
 [6] S. P. Thampi, R. Golestanian, and J. M. Yeomans, EPL (Europhysics Letters) **105**, 18001 (2014), arXiv:1312.4836.

- [7] T. Gao, R. Blackwell, M. A. Glaser, M. D. Betterton, and M. J. Shelley, *Physical Review Letters* **114**, 048101 (2015), arXiv:1401.8059.
- [8] L. Giomi, *Physical Review X* **5**, 031003 (2015), arXiv:1409.1555.
- [9] S. Shankar, S. Ramaswamy, M. C. Marchetti, and M. J. Bowick, arXiv preprint arXiv:1804.06350 (2018).
- [10] V. Narayan, S. Ramaswamy, and N. Menon, *Science* **317**, 105 (2007).
- [11] S. Zhou, A. Sokolov, O. D. Lavrentovich, and I. S. Aranson, *Proceedings of the National Academy of Sciences* **111**, 1265 (2014), <http://www.pnas.org/content/111/4/1265.full.pdf>.
- [12] T. Sanchez, D. T. N. Chen, S. J. Decamp, M. Heymann, and Z. Dogic, *Nature* **491**, 431 (2012), arXiv:1301.1122.
- [13] S. J. DeCamp, G. S. Redner, A. Baskaran, M. F. Hagan, and Z. Dogic, *Nature Materials* **14**, 1110 (2015), arXiv:1501.06228.
- [14] P. W. Ellis, D. J. Pearce, Y.-W. Chang, G. Goldsztein, L. Giomi, and A. Fernandez-Nieves, *Nature Physics* **14**, 85 (2018).
- [15] P. Guillamat, J. Ignés-Mullol, and F. Sagués, *Proceedings of the National Academy of Sciences* **113**, 5498 (2016).
- [16] Y. Luo, F. Serra, D. A. Beller, M. A. Gharbi, N. Li, S. Yang, R. D. Kamien, and K. J. Stebe, *Physical Review E* **93**, 1 (2016).
- [17] B. Senyuk, Q. Liu, S. He, R. D. Kamien, R. B. Kusner, T. C. Lubensky, and I. I. Smalyukh, *Nature* **493**, 200 (2013).
- [18] C. Peng, T. Turiv, Y. Guo, S. V. Shiyankovskii, Q.-H. Wei, and O. D. Lavrentovich, *Science Advances* **2**, e1600932 (2016), arXiv:1609.06737.
- [19] F. G. Woodhouse and R. E. Goldstein, *Physical Review Letters* **109**, 168105 (2012), arXiv:1207.5349.
- [20] T. N. Shendruk, A. Doostmohammadi, K. Thijssen, and J. M. Yeomans, *Soft Matter* **13**, 3853 (2017), arXiv:1703.01531.
- [21] T. Gao, M. D. Betterton, A.-S. Jhang, and M. J. Shelley, arXiv.org, 1 (2017), arXiv:1703.00969.
- [22] M. M. Norton, A. Baskaran, A. Opathalage, B. Langeslay, S. Fraden, A. Baskaran, and M. F. Hagan, *Physical Review E* **97**, 1 (2018).
- [23] M. Theillard, R. Alonso-Matilla, and D. Saintillan, *Soft Matter* **13**, 363 (2017).
- [24] H. Wioland, F. G. Woodhouse, J. Dunkel, J. O. Kessler, and R. E. Goldstein, *Physical Review Letters* **110**, 268102 (2013), arXiv:1304.2875.
- [25] E. Lushi, H. Wioland, and R. E. Goldstein, *Proceedings of the National Academy of Sciences* **111**, 9733 (2014), arXiv:1407.3633.
- [26] F. J. Segerer, F. Thüroff, A. Piera Alberola, E. Frey, and J. O. Rädler, *Physical Review Letters* **114**, 228102 (2015), arXiv:arXiv:1505.04643v2.
- [27] H. Wioland, E. Lushi, and R. E. Goldstein, *New Journal of Physics* **18**, 27 (2016), arXiv:1603.01143.
- [28] K.-T. Wu, J. B. Hishamunda, D. T. N. Chen, S. J. DeCamp, Y.-W. Chang, A. Fernández-Nieves, S. Fraden, and Z. Dogic, *Science* **355**, eaal1979 (2017), arXiv:1705.02030.
- [29] P. Guillamat, J. Ignés-Mullol, and F. Sagués, *Nature communications* **8**, 564 (2017).
- [30] S. P. Thampi, A. Doostmohammadi, T. N. Shendruk, R. Golestanian, and J. M. Yeomans, *Science Advances* **2**, e1501854 (2016), arXiv:1606.06563.
- [31] J. Stenhammar, R. Wittkowski, D. Marenduzzo, and M. E. Cates, *Science advances* **2**, e1501850 (2016).
- [32] S. P. Thampi, R. Golestanian, and J. M. Yeomans, *Physical Review Letters* **111**, 118101 (2013), arXiv:1302.6732.
- [33] A. U. Oza and J. Dunkel, *New Journal of Physics* **18**, 93006 (2016), arXiv:1507.01055.
- [34] R. D. Kamien, *Reviews of Modern physics* **74**, 953 (2002).
- [35] I. C. Gârlea, P. Mulder, J. Alvarado, O. Dammone, D. G. Aarts, M. P. Lettinga, G. H. Koenderink, and B. M. Mulder, *Nature communications* **7**, 12112 (2016).
- [36] G. Duclos, C. Erlenkämper, J. F. Joanny, and P. Silberzan, *Nature Physics* **13**, 58 (2017).
- [37] M. Theillard, R. Alonso-Matilla, and D. Saintillan, *Soft Matter* **13**, 363 (2017), arXiv:1608.06898.
- [38] L. M. Lemma, S. J. Decamp, Z. You, L. Giomi, and Z. Dogic, , 1 (2018), arXiv:1809.06938.
- [39] S. Chen, P. Gao, and T. Gao, *Journal of Fluid Mechanics* **835**, 393 (2018).
- [40] X. Tang and J. V. Selinger, , 1 (2018), arXiv:1809.06448.
- [41] K. Doxzen, S. R. K. Vedula, M. C. Leong, H. Hirata, N. S. Gov, A. J. Kabla, B. Ladoux, and C. T. Lim, *Integrative biology* **5**, 1026 (2013).
- [42] A. Bricard, J.-B. Caussin, N. Desreumaux, O. Dauchot, and D. Bartolo, *Nature* **503**, 95 (2013).
- [43] A. Bricard, J.-B. Caussin, D. Das, C. Savoie, V. Chikkadi, K. Shitara, O. Chepizhko, F. Peruani, D. Saintillan, and D. Bartolo, *Nature communications* **6**, 7470 (2015).
- [44] Y. H. Tee, T. Shemesh, V. Thiagarajan, R. F. Hariadi, K. L. Anderson, C. Page, N. Volkmann, D. Hanein, S. Sivaramakrishnan, M. M. Kozlov, *et al.*, *Nature cell biology* **17**, 445 (2015).
- [45] J. Brugués and D. Needleman, *Proceedings of the National Academy of Sciences* **111**, 18496 (2014).
- [46] F. Nedelec, T. Surrey, A. C. Maggs, and S. Leibler, *Nature* **389**, 305 (1997).
- [47] D. J. Needleman, M. A. Ojeda-Lopez, U. Raviv, K. Ewert, J. B. Jones, H. P. Miller, L. Wilson, and C. R. Safinya, *Physical review letters* **93**, 198104 (2004).
- [48] F. Hilitski, A. R. Ward, L. Cajamarca, M. F. Hagan, G. M. Grason, and Z. Dogic, *Physical review letters* **114**, 138102 (2015).
- [49] A. Ward, F. Hilitski, W. Schwenger, D. Welch, A. Lau, V. Vitelli, L. Mahadevan, and Z. Dogic, *Nature materials* **14**, 583 (2015).
- [50] A. Lau, A. Prasad, and Z. Dogic, *EPL (Europhysics Letters)* **87**, 48006 (2009).
- [51] W. Thielicke and E. J. Stamhuis, *Journal of Open Research Software* **2** (2014), 10.5334/jors.bl.